

## Anomalous diffraction at ultra-high energy for protein crystallography

Jean Jakoncic,<sup>a,b</sup> Marco Di Michiel,<sup>c</sup> Zhong Zhong,<sup>a</sup> Veijo Honkimäki,<sup>c</sup> Yves Jouanneau<sup>d</sup> and Vivian Stojanoff<sup>a\*</sup><sup>a</sup>Brookhaven National Laboratory, National Synchrotron Light Source, Bldg 725D, Upton, NY, USA, <sup>b</sup>Universite Joseph Fourier, Grenoble, France, <sup>c</sup>European Synchrotron Radiation Facility, Grenoble, France, and <sup>d</sup>CNRS CEA, Grenoble, France. Correspondence e-mail: vivian.stojanoff@gmail.com

Single-wavelength anomalous diffraction (SAD), multiwavelength anomalous diffraction (MAD) and single isomorphous replacement with anomalous scattering (SIRAS) phasing at ultra-high X-ray energy, 55 keV, are used successfully to determine a high-quality and high-resolution experimental electronic density map of hen egg-white lysozyme, a model protein. Several combinations, between single- and three-wavelength, with native data were exploited to demonstrate that standard phasing procedures with standard equipment and software can successfully be applied to three-dimensional crystal structure determination of a macromolecule, even at these very short wavelengths. For the first time, a high-quality three-dimensional molecular structure is reported from SAD phasing with ultra-high-energy X-rays. The quality of the crystallographic data and the experimental electron density maps meet current standards. The 2.7% anomalous signal from three Ho atoms, at the Ho *K* edge, was sufficient to obtain a remarkable electron density and build the first lanthanide structure for HEWL in its entirety.

© 2006 International Union of Crystallography  
Printed in Great Britain – all rights reserved

## 1. Introduction

To solve a *de novo* protein structure, multiwavelength anomalous diffraction (MAD) (Fourme & Hendrickson, 1990; Hendrickson, 1991) and single-wavelength anomalous diffraction (SAD) (Hendrickson & Teeter, 1981; Wang, 1985) exploit the anomalous scattering phenomena (Cassetta *et al.*, 1999; Fourme *et al.*, 1999; Hendrickson, 1999; Cianci *et al.*, 2005). Although the use of anomalous centers, either naturally occurring in metalloproteins, such as Fe and Mn, or introduced by replacement of light-metal centers, ligands or co-factors by lanthanides or organic labels containing Se and Br, was demonstrated in the early days of synchrotron radiation facilities, the real potential of the MAD and SAD methods was only realized in the past decade with significant advances in instrumentation and analytical and computational procedures. One of the major contributions to the widespread acceptance of the MAD method was the introduction of cryogenic protection of crystals, allowing extended crystal lifetime.

With the advent of third-generation synchrotrons, cryogenic protection of crystals was shown to be insufficient to prevent crystal deterioration due to radiation damage. In fact, radiation damage appears to be the major cause of unsuccessful phasing at third-generation synchrotrons (Murray & Garman, 2002). To improve protein crystal lifetime in terms of radiation damage at these facilities, experimental procedures and strategies,

such as the introduction of scavengers, alternate data collection strategies and new phasing procedures, are being developed. O'Neil *et al.* (2002) suggest that the use of glycerol or ascorbic acid as cryoprotectants prevent the formation of free radicals responsible for secondary damage such as S—S breakage and decarboxylation. Alternatively, Dauter (2002) suggested the collection of highly redundant single-wavelength (SAD) data sets, while Peterson *et al.* (1996) and González (2003) suggested the collection of two-wavelength MAD, at the inflection and high-energy remote wavelengths, instead of three-wavelength MAD sets. Another way to handle the radiation-damage issue is to treat the measured intensities mathematically, implementing an exponential decay function. Such a correction was implemented in *SHARP* (Schiltz *et al.*, 2004) and *XDS* (Diederichs, 2006). In the *SHARP* case, intensities are corrected taking into account the scatterer occupancy and *B*-factor decay, improving experimental phases only in the presence of site-specific radiation damage. Recently, Ravelli *et al.* (2003) introduced a new phasing method: radiation-damage induced phasing (RIP). Experimental phases are determined from site-specific damage, such as disulfide bond breakage or radiolytic dehalogenation of aromatic residues (Banumathi *et al.*, 2004; Zwart *et al.*, 2004). Ramagopal *et al.* (2005) further developed this method into radiation-damage induced phasing with anomalous scattering (RIPAS), combining the anomalous signal of an Hg derivative and the radiation sensitivity of Hg—S bonds

at cysteine residues, successfully to determine an unknown structure.

The advantages of a short X-ray wavelength (less than 0.33 Å) were first discussed by Helliwell & Fourme (1983) and led to the proposal to extend the wavelength range for protein crystallography beamlines at the European Synchrotron Radiation Facility (ESRF). The report further discussed the likely impact of the high-intensity beam on sample lifetime and the need of cryoprotection to avoid radiation damage. Arndt (1984) further discussed the impact of lower absorbed dose and the reduced need for absorption corrections at shorter wavelengths. Although the arguments presented in these reports were reiterated later by Helliwell (1992) and reviewed by Helliwell *et al.* (1993), only a few experiments have been reported at ~35 keV, all at third-generation synchrotrons. Single isomorphous replacement with anomalous scattering (SIRAS) at the xenon *K* edge was employed successfully by Schiltz and co-workers (Schiltz *et al.*, 1997) to determine the known structure of porcine pancreatic elastase. Recently, Takeda *et al.* (2004) employed MAD phasing at the Xe and I *K* edge of hen egg-white lysozyme derivatives. High-pressure experiments developed by Fourme's group (Fourme *et al.*, 2001, 2003; Girard *et al.*, 2004) were performed at the iodine *K* edge, 37.17 keV, to minimize scattering from the diamond anvil cell, especially at high Bragg angle, where the Compton energy shift is larger. Possible reasons for the limited use of ultra-high-energy X-rays could be the fact that this region is not readily accessible at conventional structural biology beamlines due to technical limitations of the instrumentation. On the other hand, the energy range, 5–20 keV, usually available at synchrotron beamlines, allows the choice of a wide range of anomalous scatterers, which include the *L*<sub>III</sub> edges of most lanthanides. From this perspective, there would be no advantage in collecting at ultra-high X-ray energies at the *K* edges of these elements as the anomalous power would be similar to Se and Br *K* edges. However, as shown in Fig. 1, the total linear mass absorption coefficient calculated for a

generic protein sample is about 5 cm<sup>2</sup> g<sup>-1</sup>, compared with 0.2 cm<sup>2</sup> g<sup>-1</sup> at higher energies, leading to potential lower cumulated absorbed dose; in other words, less radiation damage at high X-ray energies (Aslantas *et al.*, 2007). This could be of significant advantage in molecular structure determination of radiation-sensitive biological molecules.

To probe further the advantage of ultra-high X-ray energies in structural biology, the report below exploits the anomalous signal from Ho scatterers in tetragonal hen egg-white lysozyme (HEWL) crystals at 55.6 keV. Experiments were carried out on two high-energy beamlines dedicated to the material science community: ID15B at the European Synchrotron Radiation Facility, a third-generation machine, and X17B1 at the National Synchrotron Light Source, a second-generation facility. Phases for the two experiments were successfully calculated by three separate methods, MAD, SAD and SIRAS, to yield high-quality experimental electron density maps for modeling. For the first time, a high-quality three-dimensional molecular structure is reported from SAD phasing at ultra-high X-ray energy. The present results are discussed in the light of radiation sensitivity and phasing power, further demonstrating the usefulness of ultra-high X-ray energy crystallography.

## 2. Materials and methods

### 2.1. Sample preparation

Hen egg-white lysozyme (three times crystallized) from Sigma was used without further purification. Crystals were freshly grown 3 to 4 days prior to data collection, at room temperature, by the microbatch method under paraffin oil (Chayen, 1998). For the phasing experiments at ultra-high X-ray energies, crystals were grown in the presence of holmium. Typically, 2 µl of 100 mg ml<sup>-1</sup> hen egg-white lysozyme in 50 mM sodium acetate, pH 4.5, and 50% (v/v) glycerol was mixed with 2 µl of 0.4 M HoCl<sub>3</sub> + 1.2 M NaCl in 100 mM sodium acetate, pH 4.5; no further cryoprotection was needed. Crystals appeared in a few hours and reached a size of 400 × 400 × 300 µm within 2–3 days. Crystals used for the native data collection were grown under the same conditions in the absence of HoCl<sub>3</sub>.

### 2.2. High-energy X-ray beamlines

None of the dedicated macromolecular crystallography beamlines is capable of delivering X-rays with energies higher than 35 keV. Therefore experiments were performed at beamlines usually serving the materials science community: ID15B, at the European Synchrotron Radiation Facility in Grenoble, France (ESRF), and X17B1 at the National Synchrotron Light Source, Upton, NY, USA. Both beamlines deliver either a monochromatic beam or a white beam in the high-energy range, typically higher than 50 keV, and can accommodate a wide range of experiments; special equipment, including cryostream and an area detector, can easily be implemented.

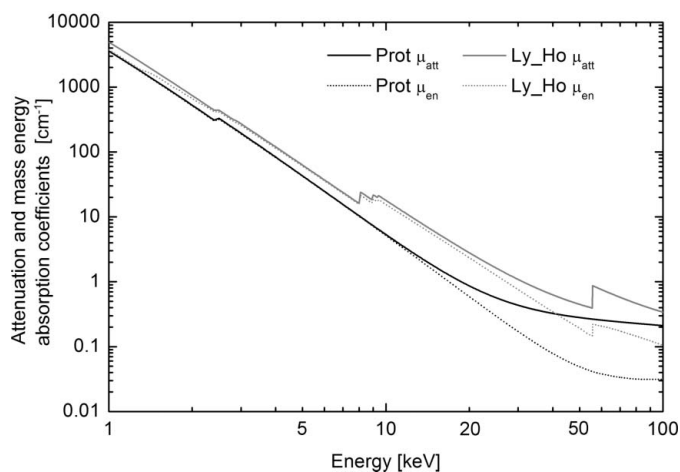


**Figure 1**

Attenuation coefficient ( $\mu_{\text{att}}$ ) and energy-absorption coefficient ( $\mu_{\text{en}}$ ) for a generic protein crystal sample (Prot) and for a holmium hen egg-white lysozyme (Ly\_Ho) derivative.

**Table 1**

Beamline parameters.

The flux is estimated at the sample position, with the used beam size at 55 keV, at 100 mA for ID15B and at 200 mA for X17B1.

	Source	Flux (photon s <sup>-1</sup> 0.1% bw) <sup>†</sup>	Beam size ( $\mu$ m)	Crystal size ( $\mu$ m)	Energy resolution dE/E <sup>‡</sup>
ID15B	Wiggler	10 <sup>12</sup> ( $3 \times 10^{13}$ )	300 $\times$ 300	400 $\times$ 400 $\times$ 300	$5 \times 10^{-4}$
X17B1	Wiggler	$4 \times 10^9$ (10 <sup>11</sup> )	300 $\times$ 300	400 $\times$ 400 $\times$ 300	$2 \times 10^{-4}$

<sup>†</sup> Numbers in parentheses refer to total integrated flux calculated with slits wide open. <sup>‡</sup> White-beam slits: 500  $\mu$ m.

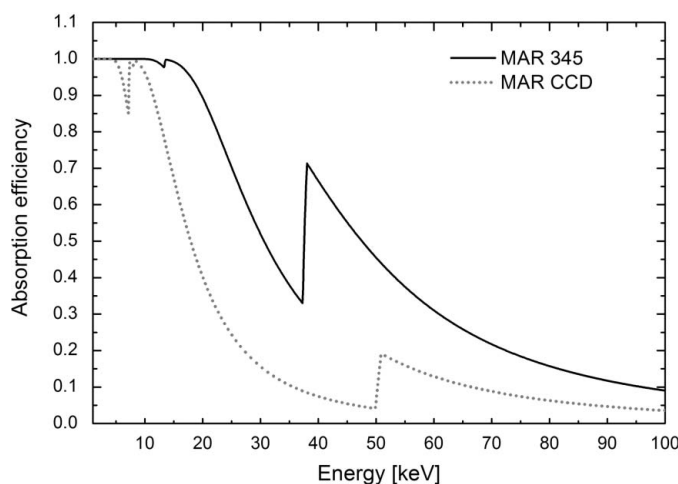
The experiment at ID15B (ESRF) was performed during the 2/3 fill mode (200 mA electron beam current); the X-ray beam was provided by an asymmetrical multipole wiggler and focused by a Bragg silicon (311) crystal monochromator (with energy resolution  $dE/E = 5 \times 10^{-4}$ ). The NSLS high-energy beamline, X17B1, is located on a superconducting wiggler. A Si (311) sagittally bent double-crystal Laue monochromator (Zhong *et al.*, 2001) focuses the beam horizontally onto the sample; the vertical beam size is typically of the order of 500  $\mu$ m. ID15B, located on a third-generation light source, generates typically a beam that is 200 times brighter than X17B1.

The strong secondary air scattering observed for the first experiments performed at both beamlines made it difficult to measure any anomalous difference from the samples accurately and completely. To minimize these effects in a second experiment and allow the accurate measurement of the anomalous signal, the initial beamstop arrangement was reviewed. On ID15B, for the first experiment, a lead beamstop of 6 mm diameter and 25 mm length was positioned on a 0.5 mm aluminium plate right in front of the detector. The sole function of this aluminium plate was to hold the beamstop; absorption is of the order of 3.5%. The diffraction patterns recorded during this first attempt all comprised a strong background that accounted for 7000 counts in the forward direction and dropped to 1000 counts in the high-resolution range. This background was reduced tremendously after the addition of a second beamstop, 2 mm in diameter and 4 mm long, also made out of lead and held on a 0.5 mm Al plate at 1/3 of the sample–detector distance. The combination of both beamstops allowed the absorption of the direct beam, suppressing secondary air scattering of low-energy X-rays from the primary beamstop and the third harmonic, as well as the remaining beam. With this arrangement, the background was 35-fold and 12-fold reduced in the low- and high-resolution ranges, respectively. On X17B1, the initial Pb beamstop, 6.4 mm in diameter and 15 mm long, mounted on a 3.2 mm thick Plexiglas plate, was positioned 10 cm from the sample, the minimum distance that still allowed sample manipulation given the beamline configuration. The Plexiglas plate absorbed 7% of the diffracted radiation. Because of its size, the beamstop was easy to align and totally absorbed the direct beam, but it did not allow collection of low-resolution data, beyond 12 Å. This lack of low-resolution data did not allow proper phasing after the substructure solution was achieved.

For the second attempt, the beamstop diameter was halved and tantalum was used for its high stopping power and machining properties. These changes allowed data to be recorded to at least 20 Å in the lowest resolution range, which ultimately enabled the first ultra-high-energy SAD phasing. Likewise, as is usual for low-energy experiments, the sample was as close as possible to the collimating slits to diminish any scattering upstream of the crystal; beam size and crystal size are shown in Table 1.

### 2.3. Detectors

Two detectors were used for data collection: at ID15B, the MAR Research 345 mm Image Plate (MAR345); at X17B1, the 165 mm MAR Research CCD (MARCCD) detector. These detectors are routinely utilized at medium energies and are not optimized for high X-ray energies. Both use a phosphor screen to image X-rays but employ different readout techniques. The MARCCD directly converts X-rays to photons in the visible spectra that are detected by a CCD. In comparison, the MAR345 uses a phosphor screen that is excited by X-rays and is read by a laser. The laser reading efficiency is significantly reduced at these high energies as it is depth dependent. Nevertheless, a naive method to characterize the detectors is through their phosphor screen absorption efficiency. The absorption efficiency of both detectors is represented in Fig. 2 for the energy range 1–100 keV. For the MAR345, a 207  $\mu$ m thick phosphor screen made from BaFBr:Eu<sup>2+</sup> (density 2.86 g cm<sup>-3</sup>) was considered, while for the MARCCD a 45  $\mu$ m thick phosphor screen made from Gd<sub>2</sub>O<sub>2</sub>S:Tb (density 2.9 g cm<sup>-3</sup>) was considered. If both detectors display efficiency greater than 80% at 12 keV, the energy commonly used for macromolecular crystallography, at 55 keV where this experiment was performed, the MAR345 absorbs 40% of the photons and the MARCCD 20%. Thus, in principle, the MAR345 would be a better choice for high-

**Figure 2**

Phosphor screen absorption efficiency for the MAR345 image-plate scanner and MAR CCD detector in the 1–100 keV range. For further discussion see text.

Table 2  
Data collection statistics.

HEWL	ID15B				X17B1			
	Native	Ho derivative			Native	Ho derivative		
Data	Native	Peak	Remote	Inflection	Native	Peak	Remote	Inflection
Wavelength (Å)	0.2227	0.2229	0.2201	0.2227	0.2227	0.2229	0.2201	0.2227
Energy (keV)		55.68	56.34	55.62		55.68	56.34	55.62
$a = b$ (Å)	78.5	78.5	78.5	78.4	79.2	78.7	78.7	78.6
$c$ (Å)	37.0	37.4	37.4	37.4	37.0	37.3	37.3	37.2
Resolution limits (Å) <sup>†</sup>	25.00–1.40	20.00–1.25	22.00–1.25	20.00–1.25	30.0–1.35	30.0–1.35	30.0–1.35	30.0–1.45
	(1.45–1.40)	(1.29–1.25)	(1.29–1.25)	(1.29–1.25)	(1.40–1.35)	(1.40–1.35)	(1.40–1.35)	(1.50–1.45)
Completeness (%) <sup>†</sup>	99.9 (100)	98.9 (100)	99.2 (100)	99.0 (100)	97.5 (97.3)	99.2 (92.4)	100 (100)	100 (99.8)
$I/\sigma(I)$ <sup>†</sup>	29.1 (5.00)	21.0 (3.5)	26.2 (4.3)	21.0 (3.5)	14.9 (2.7)	24.9 (2.1)	35.4 (3.7)	19.2 (2.3)
$R_{\text{merge}}$ (%) <sup>†‡</sup>	9.2 (48.4)	10.3 (60.0)	9.8 (63.5)	9.5 (61.4)	8.8 (44.2)	7.3 (75.3)	6.7 (73.7)	7.9 (69.3)
Mosaicity (°)	0.15	0.25	0.25	0.25	0.1	0.46	0.47	0.46
Total no. of reflections	453777	453706	748407	455949	191991	321800	565274	177785
Redundancy	10.4	7.4	12.2	7.4	4.0	6.5	11.5	4.5
No. of unique reflections	43620	61274	61396	61272	48169	49334	49081	39880
$\Delta_{\text{ano}}/\sigma(\Delta_{\text{ano}})$ <sup>§</sup>		1.0 (1.7)	1.0 (1.6)	0.8 (3.6)		0.9 (2.0)	1.0 (1.8)	0.7 (5.0)
No. of frames	240	180	360	180	90	180	360	120

<sup>†</sup> Numbers in parentheses refer to the highest resolution shell. <sup>‡</sup>  $R_{\text{merge}} = \sum_h \sum_i |I(h)_i - \langle I(h) \rangle| / \sum_h \sum_i I(h)_i$ , where  $I(h)_i$  is the  $i$ th observation of reflection  $h$  and  $\langle I(h) \rangle$  is the mean intensity of that reflection. <sup>§</sup> Overall value while the number between parentheses refers to the resolution (Å) where  $\Delta_{\text{ano}}/\sigma(\Delta_{\text{ano}})$  crosses 1.0.

energy measurements, as it presents a better efficiency, better dynamic range and larger size.

2.4. Energy scan

For both beamlines the energy was calibrated at the holmium *K* edge (55.618 keV) with the crystallization stock solution containing holmium chloride. The three wavelengths selected for the MAD experiment, 0.2229, 0.2227 and 0.2200 Å (55.62, 55.68 and 56.34 keV), namely inflection, peak and high remote, respectively, were determined from the absorption spectra measured by the fluorescence method on the solution using an ion chamber. Fig. 3 displays the variation of scattering factors  $f''$  and  $f'$  with energy according to the absorption spectrum recorded on the stock solution at ID15B. The dotted arrows show the energies at which the data were actually collected; the plain arrows correspond to the peak and

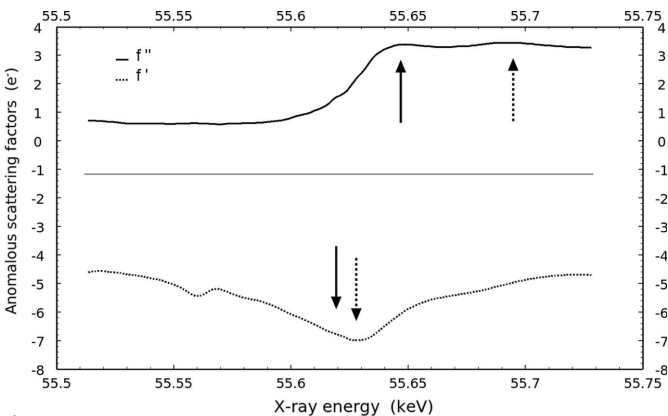


Figure 3  
Fluorescence energy scan recorded on the holmium chloride stock solution used for crystallization. The spectra were normalized with  $I_0$  and processed with *CHOOCH* (Evans & Pettifer, 2001). The dotted arrows indicate the peak and inflection energies as determined by *CHOOCH*; the plain arrows indicate the actual energies selected for data collection: 55.62 keV (0.2229 Å), 55.68 keV (0.2227 Å); the energy used for the remote data collection [56.34 keV (0.22 Å)] is not shown.

inflection energies if the energies determined by *CHOOCH* (Evans & Pettifer, 2001) were adopted.

The crystals were directly recovered from the crystallization drop and mounted in a random orientation on the goniometric head. The sample was maintained at a temperature of 100 K by a nitrogen cold stream (Oxford Cryosystem series 600) throughout the experiment. Data were recorded using the rotation method. On ID15B, the sample to detector distance was chosen to allow for data collection up to 0.91 Å resolution at the boarder of the image plate. 180 frames, corresponding to a total of 180° in oscillation range, were recorded at the peak energy, followed by 360 frames at the high-energy remote and finally 180 at the inflection energy, bearing in mind the MAD phasing procedure and the maximization of the dispersive signal at the inflection energy in case of radiation damage. A single-wavelength experiment at the peak energy position was carried out on a second crystal for experimental redundancy; these data are not shown. On X17B1, the MAR CCD detector was placed at a distance of 400 mm from the sample. The same data collection strategy was followed, except that 120° were collected at the inflection energy due to beam time limitations. Exposure time per frame was 4 s on ID15B, while 100 s per degree were required at X17B1. Details of the various data collection runs are given in Table 2. An estimate of the absorbed dose for each experiment is presented in Appendix A. In both cases, an additional data set was collected on a native lysozyme crystal at 0.2227 Å wavelength for phasing purposes.

2.5. Data processing, phasing and refinement

The recorded intensities were integrated, scaled and merged with the *DENZO/SCALEPACK* suite (Otwinowski & Minor, 1997) and were converted into amplitudes for further analysis using *TRUNCATE* (French & Wilson, 1978). These data were used in the determination of experimental phases by three different methods: SIRAS, MAD and SAD. Experi-

mental phases were determined from several combinations between single- and three-wavelength, with and without consideration of native data. In these studies, the *SHELX* package (Sheldrick & Gould, 1995) was used to locate the heavy-atom positions by the powerful dual-space recycling principle as implemented in *SHELXD*, followed by a few density modification cycles with *SHELXE*. The successful use of other software suites, either just to locate the Ho sites, or for phasing, such as, *CRANK* (Ness *et al.*, 2004) and the *CCP4* suite (Collaborative Computational Project, Number 4, 1994) used for SAD phasing at the high-energy remote (56.34 keV) and at the peak (55.68 keV), or *HYSS* (Grosse-Kunstleve & Adams, 2003; *Phenix* collaboration) used to locate the Ho sites for the three-wavelength MAD data and SAD data, further demonstrate the applicability of standard phasing procedures (software) to ultra-high X-ray energy data. Further density improvement was performed using *DM* (Cowtan, 1994) with a 40% solvent content and calculated Matthews's coefficient of  $2.06 \text{ \AA}^3 \text{ Da}^{-1}$  (Matthews, 1968). This modified density served as input to *ARP/wARP* (Perrakis *et al.*, 1999) for automated chain tracing. The refinement was performed with *REFMAC* (Murshudov *et al.*, 1997). Electron density maps and refined models were inspected with *COOT* (Emsley & Cowtan, 2004), which also allowed manual building and manual reconstruction of the missing parts.

### 3. Results and discussion

#### 3.1. Crystals and diffraction quality

Although previous experiments (Gonzalez *et al.*, 1994; Schiltz *et al.*, 1997; Takeda *et al.*, 2004), performed at macromolecular crystallography beamlines with a fixed and pre-

aligned beamstop, indicated that background noise did not seriously affect data collection and processing, initial experiments carried out on both beamlines, ID15B and X17B1, did not allow the determination of the molecular structure with any of the phasing methods being considered. In spite of the reasonable diffraction quality of the images and scaling results, it was possible to find only two out of the three Ho sites, following the procedure described in §2.5. However, it was impossible to obtain an interpretable experimental electron density map, much less obtain a model for the molecular structure. To improve the signal-to-background ratio and the statistics, an additional beamstop was installed on X15B and a smaller beamstop was used on X17B1. The use of this additional beamstop on ID15B led to the reduction of the background by a factor of 10. On X17B1, the use of the smaller beamstop allowed the collection of data in the low-resolution shells. The use of these two improved beamstop configurations ultimately produced the first structure of a protein crystal at energy higher than 40 keV using current experimental phasing methods. The data collection statistics presented in Table 2 are the result of a second set of measurements obtained with these improved beamstop configurations.

All the crystals measured belong to the tetragonal space group  $P4_32_12$  with unit-cell parameters of the order of  $a = b = 78$ ,  $c = 37 \text{ \AA}$ , and exhibit rather low mosaicities. Even if crystals diffracted well beyond  $1.3 \text{ \AA}$ , the diffraction limits reported are a good compromise between exposure time, detector readout and allocated beam time. Fig. 4 displays sections of a typical diffraction patterns obtained at both beamlines. Data quality, as judged from the statistics [resolution, mosaicity,  $I/\sigma(I)$ , completeness and  $R_{\text{merge}}$ ], meets current standards. The values presented in Table 2 are in good agreement with recently reported values for HEWL structures determined to

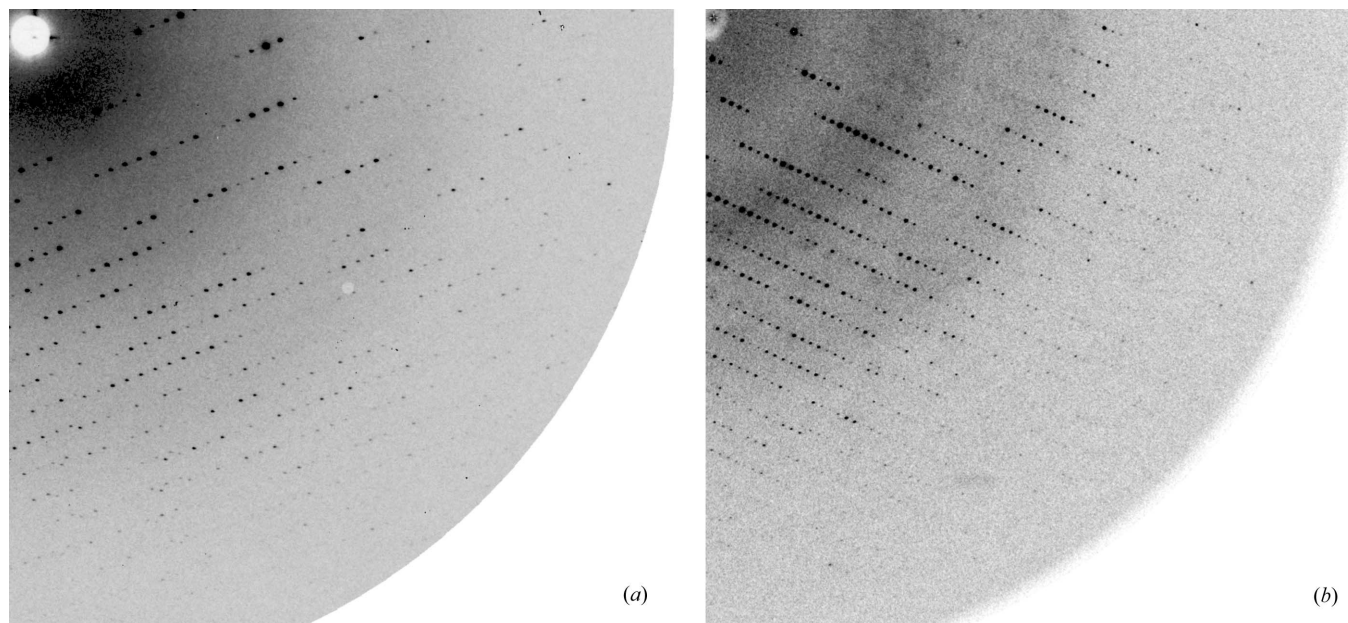


**Figure 4**

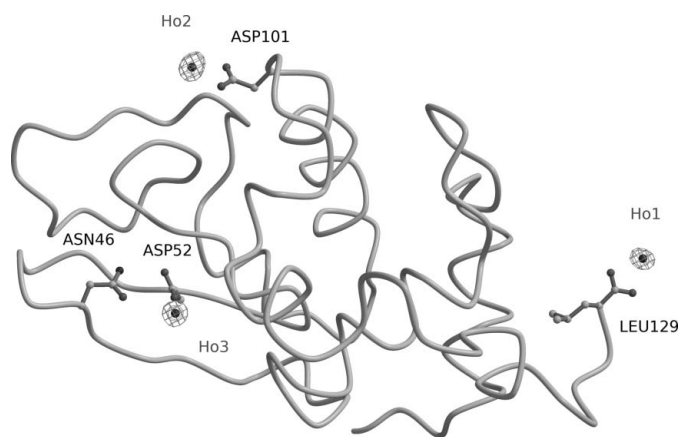
Typical diffraction pattern recorded on (a) a MAR CCD 165 mm detector at the X17B1 beamline (sample to detector distance 400 mm and wavelength  $0.2153 \text{ \AA}$ ; the resolution at the edge is  $1.35 \text{ \AA}$ ); (b) a MAR 345 scanner at the ID15B beamline (sample to detector distance of 850 mm and wavelength  $0.219 \text{ \AA}$ ; the resolution at the edge is  $1.15 \text{ \AA}$ ).

**Table 3**

Phasing results.

The correlation coefficients (CC) for the maps are calculated using the electron density after density modification with the model built and partially refined as provided by *ARP/wARP* at the model-building stage for each method. The refined model (PDB access code 2CGI) was refined taking into account the native and the Ho remote data collected on ID15B (Table 2).

		ID15A			X17B1		
		MAD <sub>+nat</sub>	SIRAS <sub>pk</sub>	SIRAS <sub>rm</sub>	SAD <sub>pk</sub>	SAD <sub>rm</sub>	SIRAS <sub>pk</sub>
<i>SHELXD</i>	Correct/total trials	14/30	17/30	15/30	19/30	29/30	22/30
	CC/contrast	0.75/0.40	0.69/0.42	0.72/0.42	0.77/0.47	0.80/0.47	0.71/0.40
<i>SHELXE</i>	Connectivity	0.89	0.9	0.88	0.89	0.89	0.88
	FOM	0.81	0.79	0.79	0.75	0.77	0.8
	Map CC	0.83	0.76	0.8	0.89	0.85	0.77
<i>ARP</i>	Res built (AA/wat)	127/162	128/164	128/156	124/162	125/162	126/171
	R/R <sub>free</sub> (%)	20/23	20/23	21/25	24/27	25/28	20/24
Model refined	PDB access code			2CGI	2BPU		
	R/R <sub>free</sub> (%)			17.5/19.5	17.1/19.5		

**Figure 5**

Anomalous difference map, contoured at the  $11\sigma$  level, after density modification (Cowtan, 1994); SAD phasing of high-energy remote (56.34 keV, *i.e.* 0.22 Å) data collected on X17B1. The main-chain trace and ligand residue side chains are shown. The figure was produced with *BOBSCRIPT* (Esnouf, 1997; Kraulis, 1991) and enhanced with *RASTER3D* (Merritt & Murphy, 1994).

similar resolutions on standard macromolecular crystallography beamlines in the medium-energy range (for example, PDB access code 2C8O and 1QIO). The higher  $R_{\text{merge}}$  values observed here are attributed to systematic and experimental errors and might be expected as this experiment was carried out on non-dedicated beamlines. To verify the quality of the data, a complete data set was collected at medium energy (12 keV) on a standard macromolecular crystallography beamline (Allaire *et al.*, 2003) on a crystal grown under the same conditions and of the same size. Similar diffraction resolution with a 4 s exposure per oscillation resulted in similar statistics with an  $R_{\text{merge}}$  of 4.5%, compatible with the values reported in the PDB for the structures mentioned above. The quality of the electron density map after density modification was also shown to be of the same quality as those in Figs. 5 and 6. The higher  $R_{\text{merge}}$  value observed for the data collected at high energy can then be traced back to the experimental setup. Most probably, the main causes for error are shutter-rotation timing, rotation deviations, *etc.* Analysis

of the diffraction patterns and data processing did not show any visible onset of radiation-damage effects.

### 3.2. Phases and electron density maps

The three-wavelength data and the native data set collected on each beamline were exploited to test the viability of different standard phasing methods used with medium energy for ultra-high X-ray energies. MAD phasing was performed employing three (Hendrickson & Teeter, 1981) and two wavelengths (peak and remote, peak and inflection, inflection and remote) (González, 2003). Heavy-atom positions were determined from the anomalous signal for SAD (peak and remote) and MAD phasing three- and two-wavelength combinations. For SIRAS phasing, the data obtained for the peak and remote wavelengths were combined with the native data, while SAD phasing was performed on each of the individual wavelengths, peak and remote. Three strong peaks corresponding to the Ho sites were identified in all the calculated anomalous difference maps. The anomalous difference map obtained from the high-energy remote (56.64 keV) data collected on X17B1 is shown in Fig. 5. The map, contoured at the  $11\sigma$  level, indicates the presence of three holmium sites with strong anomalous signal. The phasing quality obtained for the different methods employed is summarized in Table 3; not all the results are shown for both beamlines, as the phasing qualities are similar for the same method. According to statistics shown in Table 3, all the methods, SIRAS, MAD and SAD, were successful, presenting high figures-of-merit (FOM) and connectivity, independent of the phasing method. Phasing with the *SHELX* suites (Sheldrick & Gould, 1995), *SHELXD* and *SHELXE*, was as successful as in the medium-energy cases (12 keV range) for processing high-resolution data. The use of different software suites, *HYSS*, *PHENIX*, *CRANK*, *CCP4* (Ness *et al.*, 2004; Grosse-Kunstleve & Adams, 2003; Collaborative Computational Project, Number 4, 1994), to phase MAD data was as successful, presenting high figures-of-merit and good correlation factors. These results are not presented, as the comparison between software suites is not the purpose of this report. Thus, for phasing to succeed at ultra-high X-ray energies,

similar requirements as found in the medium-energy cases (12 keV range) need to be observed.

Fig. 6 represents the experimental electron density maps calculated by the three different methods under consideration, SIRAS, MAD and SAD. The maps after density modification exhibited not only main chains but also most of the side chains and water molecules. Models were built in full using the *ARP/wARP* program suite. They were all at least 95% complete and accurate, as attested by the high correlation coefficients listed in Table 3. Poor electron density was observed only for highly flexible regions including the C and/or N terminal residues and the loop extending from Pro70 through Ser72. Missing residues were manually added and two models fully refined and deposited in the Protein Data Bank; one resulting from the SIRAS phasing method using the high-energy remote and native data sets collected at 0.22 Å on ID15B (PDB access code 2CGI), and the second from SAD phasing at the Ho peak energy collected on X17B1 (PDB access code 2BPU). The SIRAS crystallographic model was refined at 1.35 Å resolution to an *R* factor of 17.5% and *R*<sub>free</sub> of 19.5%; *R*<sub>free</sub> was calculated from 5% of all the reflections. The model consists of the complete chain, one Cl<sup>−</sup> ion and 215 water molecules. None of the residues was found in the disallowed region of the Ramachandran plot and the low root-mean-square (r.m.s.) deviations from ideal bond lengths and angles, 0.007 Å and 1.1°, are a confirmation of a good stereochemical agreement. The SAD model, refined to an *R* factor of 17.1% and *R*<sub>free</sub> of 19.5%, consists of the complete chain, three Ho<sup>3+</sup> ions, one Na<sup>+</sup> ion, three Cl<sup>−</sup> ions and 107 water molecules. As for the SIRAS model, no residues were found in the disallowed regions of the Ramachandran plot and, as before, the low values found for the stereochemical deviations in bond lengths and angles are 0.007 Å and 1.1°. Both models were compared to a native hen egg-white lysozyme structure (PDB access code 2BLX) determined from medium-energy data (wavelength 0.94 Å) and with similar diffraction resolution (1.4 Å) (Nanao *et al.*, 2005). The r.m.s. deviations between the main C<sup>α</sup> chains were found to be 0.21 Å and 0.13 Å for the SIRAS and SAD models, respectively, with the largest differences being observed at the C terminal and the loop region. The overall *B* factors, 13.6 Å<sup>2</sup> for the SIRAS and 12.8 Å<sup>2</sup> for the SAD model, are comparable with the native structure used for comparison, with an overall *B* factor of 10.1 Å<sup>2</sup>; relative variations of individual *B* factors are also similar. Identical results were obtained when the *K*-edge SAD structure was compared with a structure (data not presented) determined by single-wavelength anomalous phasing of data collected at a wavelength of 1 Å on similar crystals on a standard macromolecular crystallography beamline (Allaire *et al.*, 2003). The phasing and refinement results found for both structures, SIRAS and SAD, are quite similar to those obtained by Takeda's group (Takeda *et al.*, 2004) from MAD phasing data collected on the *K* edge of HEWL xenon (PDB access code 1VAU) and iodine (PDB access code 1VAT) derivatives. Although the occupancy was quite low for both these derivatives (I and Xe), MAD phasing allowed to distinguish between the protein and solvent regions prior to any density

modification, but not to build the structure model. In the present study, MAD phasing of the HEWL Ho derivative resulted in an experimental electron density map of sufficient quality to trace the molecular model; most of the main and side chains could be traced automatically. Raw SAD phases, before any density modification from either *SHELXE* or *DM*, also proved to be sufficient to build a nearly complete model; however, density modification improved the phases and allowed automated construction of most of the model in only five cycles in *ARP/wARP*, in comparison with the 15 cycles necessary without *DM* application. The overall correlation coefficients of the maps, FOM, determined from SAD phasing for the high-energy remote case with and without the application of density modification, and for the refined model were 0.85 and 0.60, respectively.

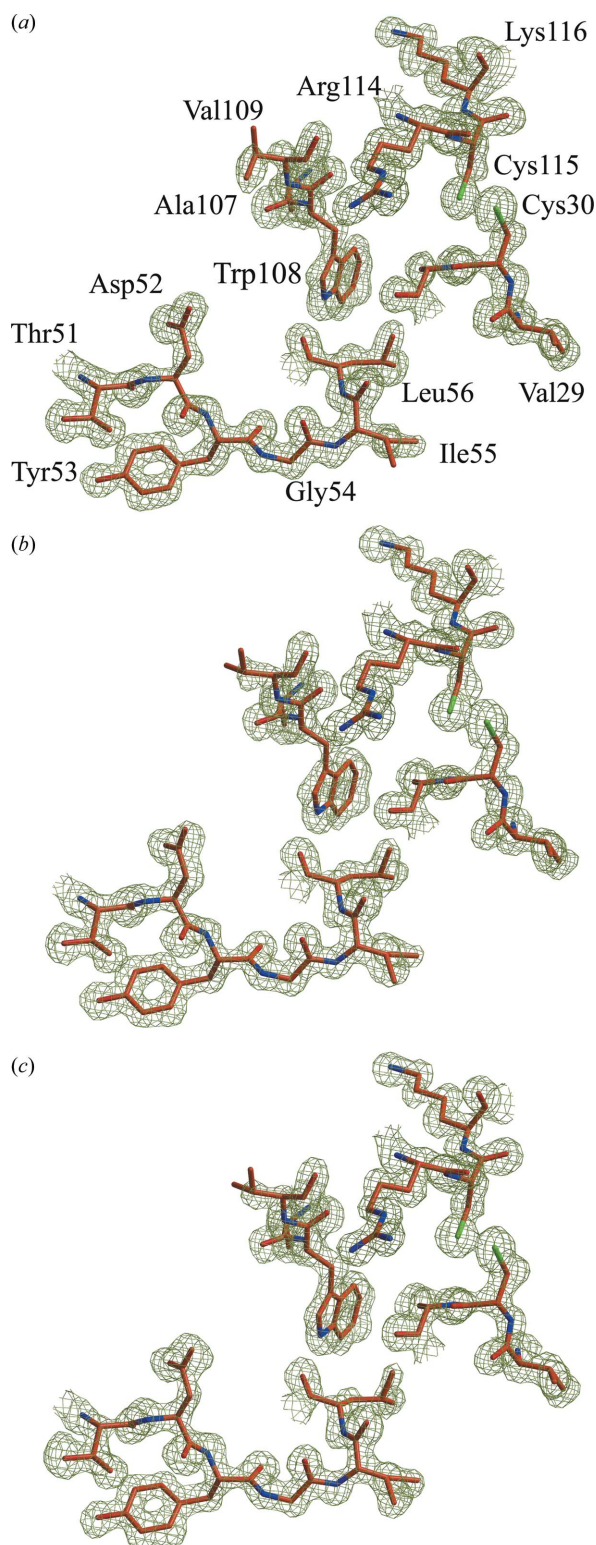
### 3.3. The holmium sites

Three Ho sites, Ho-1, Ho-2 and Ho-3, were found in the present holmium HEWL derivative, as shown in the anomalous difference map in Fig. 5. During refinement, site occupancies converged to 0.3, 0.8 and 0.5 for Ho-1, Ho-2 and Ho-3, respectively. The contribution to the anomalous signal at these refined occupancy levels is 2.7%, compared with the expected 3.9% for fully occupied sites. The holmium site Ho-1 is located on a crystallographic twofold axis. Ho-1 binds to the main-chain oxygen of residue Leu129 of the C terminus and the oxygen of one water molecule and the symmetry-related residue and water molecule. The Ho-2 site, located at the solvent boundary, binds to the Asp101 side-chain oxygen and four water molecules. The third site, Ho-3, located in the catalytic cleft, binds to Asp52 side-chain OD2 atom and five water molecules; Ho-3 is 7 Å away from the closest symmetry-related residue, Arg21. In general, poor electron density was observed around positively charged and hydrophobic side chains in close vicinity to these holmium sites; for example, no density was observed for the side chains for residues Arg21 and Val109. As frequently reported in the literature, holmium sites are usually hexacoordinated, often binding to the side-chain oxygen atom of acidic amino acids and on occasions to the carbonyl atom from the main chain. The three holmium sites found here are also hexacoordinated by oxygen atoms, but in the present case by oxygen atoms belonging to water molecules.

### 3.4. SAD phasing and redundancy

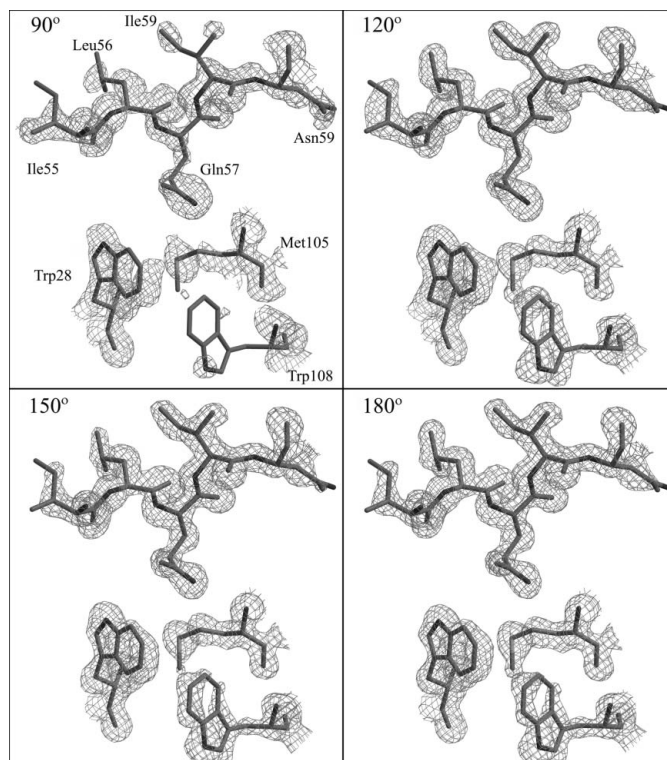
One of the limiting factors in the SAD phasing method is the accurate measurement of intensities that will result (if anomalous scatterers are present with relatively high occupancy) in accurate heavy-atom positions and good phase estimates (Dauter *et al.*, 1999). For this purpose, redundancy study was performed on the Ho *K*-edge peak data recorded at X17B1. Starting with the 180° data set initially recorded; 90, 120 and 150° data were generated at the scaling stage. Table 4 shows the statistics from the scaled data and the phasing–model-building steps. All data were scaled to the highest resolution reported for the 180° data, 1.35 Å. Fig. 7 displays



**Figure 6**

Experimental electron density maps. The maps are calculated after phasing and density modification; all maps are contoured at the  $1\sigma$  level. (a) SAD phasing at the peak wavelength (0.2227 Å) using data recorded on X17B1. (b) SIRAS phasing with the high-energy remote (0.22 Å) and native data recorded at ID15B; residues shown as labelled in (a). (c) Three-wavelength MAD (peak, inflection and high-energy remote) phasing combined with native data recorded on ID15B; residues shown as labelled in (a). The figure was produced with *MOLSCRIPT*, *BOBSCRIPT* and *RASTER3D*.

the four calculated maps after density modification was performed. For the 90° generated data set, with sixfold redundancy in the whole resolution range and twofold redundancy in the highest resolution shell (due to low completeness), it was not possible to build a complete model, whereas for the 120° data, with 7.5- and 3.5-fold redundancies for the full range and highest resolution shell, it was possible to build a 107 amino acid model, which represents 82% of the complete model. The last generated data set, 150°, and the 180° data set, were highly redundant over the full range as well as in the last resolution shell. It was possible therefore to build the complete model except for the loop region, residues 69–72, and the C and N terminus residues. Similar results were obtained with data collected on a crystal grown in the same condition with the same size at the high-energy remote (1.0332 Å, 12 keV, with  $f'' = 8.7 e^-$ ) of the  $L_{III}$  holmium edge where a 120° total oscillation range (4.4-fold redundant and 97% complete in the full resolution range due to a square detector, ADSC Q210) yielded a 1.35 Å resolution, complete model, except for the loop containing residues 71–73, and the C and N terminus residues. Thus, as with low-energy data, redundancy (Dauter & Adams, 2001) is a limiting factor for structure determination by SAD phasing at ultra-high X-ray energies. However, the same amount of data recorded at ultra-

**Figure 7**

The electron density map generated after ten cycles of density modification performed on the data collected at the peak wavelength of the Ho K edge on beamline X17B1 is shown superimposed on the refined SAD model. The corresponding crystal rotation range within the total amount of data recorded (180°), used to obtain the electron density maps shown, is indicated in the top left corner of each panel. Residues shown are indicated in the top left panel. The resolution of the map is 1.35 Å and the corresponding redundancy is indicated in Table 4. The figure was produced in the same way as Fig. 6.



**Table 4**

SAD phasing statistics.

Data sets with different completeness and redundancy were generated from a single data set; for further discussion see text. Numbers in parentheses refer to the highest resolution shell (1.37–1.35 Å).

Number of frames processed	90	120	150	180
Completeness (%)	92.9 (62.9)	97.9 (70.9)	99.0 (83.0)	99.2 (86.1)
Unique reflections	24737 (822)	26052 (926)	26365 (1084)	26419 (1124)
Total reflections	147263	195059	251843	315976
Redundancy	6.0 (2.0)	7.5 (3.5)	9.6 (4.1)	12.0 (5.1)
$I/\sigma(I)$	22.6 (1.6)	24.2 (1.7)	28.7 (1.9)	32.6 (2.1)
$R_{\text{merge}}$ (%)	6.8 (68.9)	7.1 (73.1)	7.4 (74.6)	7.8 (79.9)
FOM <sub>dm</sub> †	0.72	0.76	0.77	0.78
MAP <sub>corr</sub> ‡	0.58	0.72	0.75	0.74
RES <sub>built</sub> §	10	107	126	122

† Figure of merit calculated after density modification performed by *DM*. ‡ The map correlation is calculated between the map after density modification and the deposited structure calculated from the complete peak data devoid of water molecules and ions. § Number of residues built with *ARP/wARP* starting with the structure factors and phases from *DM*.

**Table 5**

Dose estimate for crystals of similar size, and diffraction resolution and intensities, exposed to ultra-high X-ray energies (ID15B and X17B1) and to medium X-ray energies (X6A).

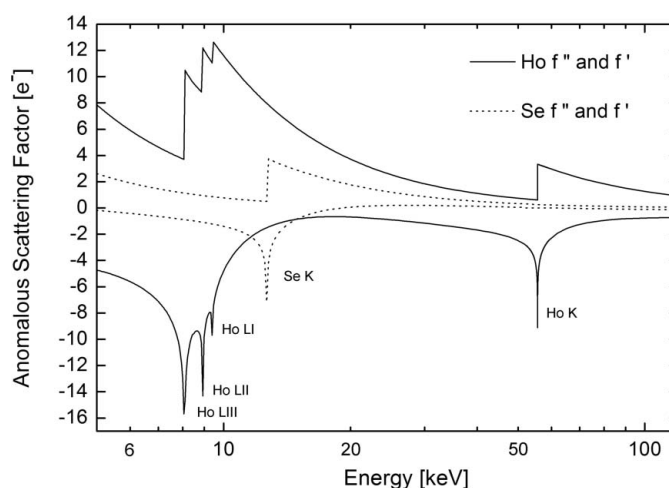
	ID15B†	X17B1†	X6A‡
Energy (J)	$8.91 \times 10^{-15}$	$8.91 \times 10^{-15}$	$1.92 \times 10^{-15}$
Flux (photon s <sup>-1</sup> ) at sample	$1.8 \times 10^{11}$	$9 \times 10^9$	$9 \times 10^{10}$
Time (s) per data set§	360	9000	360
( $\mu_{\text{en}}/\rho$ ) (cm <sup>2</sup> g <sup>-1</sup> )	0.17	0.17	7.3
Dose (J kg <sup>-1</sup> )¶	98	123	454

† Data collected at the high-energy remote Ho *K* edge wavelength, 0.22 Å (56.3 keV). ‡ Data collected at the high-energy remote Ho *L* edge wavelength, 1.03 Å (12.0 keV). § Total exposure time per data set. The data set is 90 frames of 1° oscillation. ¶ To obtain the actual dose deposited, it is necessary to consider the actual crystal cross section with the beam during data collection.

high (55.6 keV) and medium (12 keV) energy resulted in a similar model with equivalent quality and a lower deposited dose (Table 5).

### 3.5. Phasing at ultra-high X-ray energies

The *K*-edge anomalous scattering factor for lanthanides is of the same order as the Se *K*-edge scattering factor, making them ideal candidates for anomalous scattering experiments at ultra-high X-ray energies. Fig. 8 shows the scattering factors for holmium and selenium in the medium- and high-energy range. If Ho  $f''$  at its *L* edges is very attractive ( $\sim 12$  e<sup>-</sup>), when possible it is preferable to collect data at higher energy, *i.e.* 13 keV, where  $f''$  is still high ( $\sim 7$  e<sup>-</sup>), and the dose deposited on the crystal is expected to be lower due to the lower mass absorption coefficient (30 cm<sup>2</sup> g<sup>-1</sup> m<sup>-1</sup> at 9 keV and 10 cm<sup>2</sup> g<sup>-1</sup> m<sup>-1</sup> at 13 keV; Fig. 1). Therefore, ultra-high X-ray energies should further lower the expected dose deposited on the crystal and extend its lifetime. Consequently, Ho, like transition elements and other lanthanides, should be useful in a wide energy range for phasing purposes. At the Ho *K* edge, the contribution to the anomalous signal is 3.3 e<sup>-</sup>, which would be sufficient (with minimal data errors) to estimate phases for a 200 amino acid protein with only one fully occupied holmium atom site with a theoretical Bijvoet ratio of 1.7%. Several successful phasing experiments were reported for anomalous signals as small as 0.6% in the medium- and low-energy ranges for high accuracy, *i.e.* high-redundancy data

**Figure 8**

Anomalous scattering factors in the 4–120 keV range for holmium and selenium. The contribution to the anomalous signal at the *K* edge is nearly the same for both elements and other lanthanides. Consequently, Ho is useful in a wide range of energy for phasing purposes (<http://lipro.msl.titech.ac.jp/scatfac/scatfac.html>).

(Wang, 1985; Ramagopal *et al.*, 2003). Similar contributions to the anomalous signals are expected at the ultra-high X-ray energy range for commonly used derivatives such as bromide and mercury. Dauter & Dauter (1999) used the anomalous signal of the bromine *K* edge for the determination of experimental phases of a lysozyme molecule. At 50 keV, the expected Bijvoet ratio ( $\langle \Delta F^{\text{anom}} \rangle / \langle F \rangle$ ), *i.e.* anomalous contribution, of the six bromine atoms, located in the solvent shell, refined to full occupancy, would be of the order of 0.6% (calculated with  $f'' = 0.37$  e<sup>-</sup> at 50 keV). Based on error-free data, Wang (1985) estimated that for S and  $\langle \Delta F^{\text{anom}} \rangle / \langle F \rangle$  as low as 0.6%, it would be possible to solve a structure by the SAD method. Indeed, Ramagopal and co-workers (Ramagopal *et al.*, 2003) confirmed this prediction experimentally, concluding that Wang's conjecture was realistic. Recently Ramagopal *et al.* (2005) have shown that Hg derivatives are quite sensitive to radiation damage. At 55 keV,  $f'' = 1.3$  e<sup>-</sup> and the expected contribution to the Bijvoet ratio is of the order of 1% per Hg atom per 95 residues, which would be sufficient for structure solution by the SAD technique.

### 3.6. Potential future for ultra-high-energy crystallography

The potential application of ultra-high-energy phasing is quite broad. Dedicated beamlines and experimental setups would further reduce systematic errors, while the development of systematic data collection strategies (Fourme *et al.*, 2003) will allow significant gain in the signal-to-noise ratio. The generated increase in internal data consistency would allow the exploitation of difficult problems such as the measurements of small anomalous signals, or small radiation-sensitive or poorly diffracting crystals.

Currently none of the dedicated macromolecular crystallography beamlines is capable of providing X-rays with energies higher than 40 keV. Thus, if crystallographers are interested in collecting data at ultra-high energy, new high-energy macromolecular beamlines should be planned. New synchrotrons are being built in Europe (SOLEIL, DIAMOND) and existing synchrotrons are being upgraded in the USA (SSRL, ALS). New facilities with ultra-bright/ultra-focused beams are also planned in the USA (NSLSII). These new or upgraded light sources could eventually provide ultra-intense/bright/focused high-energy X-ray beams if such a need is made known to the designers. To our knowledge, no such beamline for macromolecular crystallography is planned at any of the facilities listed above.

Current detectors are also not optimized for high-energy data collection. It should be relatively straightforward to mount an adequate phosphor layer on a CCD detector, thus optimizing the detector absorption efficiency and reducing the exposure time required per oscillation range, further minimizing the radiation damage incurred. With an optimized source, an implemented macromolecular crystallography experimental setup and high-energy optimized detectors combined together, it will be possible to collect almost ideal high-quality data (Helliwell *et al.*, 1993) without radiation damage, nearly free of absorption errors.

## 4. Conclusion

This study has demonstrated that anomalous scattering at ultra-high X-ray energies is a viable alternative to the solution of the phase problem in macromolecular crystallography. For the first time, the anomalous signal from the *K* edge of a lanthanide was employed to probe several phasing methods, namely single isomorphous replacement with anomalous scattering (SIRAS), multiwavelength anomalous diffraction (MAD) and single-wavelength anomalous diffraction (SAD), and a high-resolution high-quality three-dimensional molecular model was obtained from single anomalous diffraction phasing (SAD) at ultra-high X-ray energies. Two distinct measurements were carried out on ultra-high X-ray energy beamlines located at a third-generation synchrotron facility, ID15B at the European Synchrotron Radiation Facility, and at a second-generation synchrotron facility, X17B1 at the National Synchrotron Light Source. In spite of non-optimized beamline instrumentation, detectors and software, the high quality of the data measured provided experimental electron

density maps of comparable quality to the maps obtained in the medium-energy regime (12 keV). Dose estimation showed that even with poor detector performances, there is a clear advantage to be gained by recording data at higher energies as the lifetime of the crystal is extended, while maintaining data quality. This study represents one more step towards the measurement of the 'ideal data set' (Helliwell *et al.*, 1993; Fourme *et al.*, 2003) and the efficient exploitation of the anomalous signal at ultra-high X-ray energies.

## APPENDIX A

### Dose estimation

In order to better assess the benefits and drawbacks of conventional data collection at ultra-high X-ray energies, it is interesting to compare the doses deposited in the sample during data collection at the two beamlines. These results are further compared with those found for a similar crystal submitted to data collection at a bending-magnet beamline at a second-generation synchrotron at medium energy (12 keV). To estimate the dose presented in Table 5, the energy-absorption coefficient ( $\mu_{\text{en}}$ ) rather than the absorption ( $\mu$ ) or attenuation coefficients ( $\mu_{\text{att}}$ ) was considered, as at higher energies (>30 keV) Compton scattering is predominant. Fig. 1 shows the mass attenuation as well as the mass energy-absorption coefficients for a generic protein crystal sample and for the refined model protein (lysozyme, with solvent molecules, Na, Cl and Ho ions) as a function of energy; the mass absorption coefficient, not shown, is very close to the attenuation coefficient.

Taking into account the crystal and beam size, the dose deposited on the samples is proportional to

$$D = \left( \frac{\mu_{\text{en}}}{\rho} \right) \text{Fl} E T N 1000 \text{ (Gy)},$$

where Fl is the fluence, expressed in photons  $\text{s}^{-1} \text{cm}^{-2}$ ;  $\mu_{\text{en}}/\rho$  is the mass energy-absorption coefficient in  $\text{cm}^2 \text{g}^{-1}$ ;  $E$  is the energy in J (energy in eV  $\times$  electron charge =  $1.6 \times 10^{-19}$  J);  $T$  is the exposure time in s;  $N$  is the number of frames recorded per data set. For the three experiments, the two high-energy experiments on X15B and X17B1, and for the medium-energy experiment on X6A, the same beam size and crystals of approximately the same size were chosen. In this case, the above equation can be simplified and the estimated dose is proportional to  $(\mu_{\text{en}}/\rho) \text{Flux} E T$ , with Flux being the flux at the sample determined experimentally by ion chamber at the given energy; the dose is then determined neglecting crystal rotation. The difference between the results obtained for the two high-energy experiments is due to the detector type used: the MAR345 is much more efficient for the energy range used here, 55 keV, than the MARCCD, and therefore a shorter exposure time is required to reach the same resolution limit and diffraction intensity. It is clear from the estimates shown in Table 5 that to obtain the same diffracting power, the dose deposited in the sample at medium energy is significantly higher than that deposited at ultra-high X-ray energy.

We would like to thank D. P. Siddons for valuable discussions and T. Buslaps for supporting this project. We acknowledge the European Synchrotron Radiation Facility for provision of synchrotron radiation facilities. We thank R. Greene and the staff of the National Synchrotron Light Source. The NSLS is supported by the US Department of Energy, Office of Basic Energy Sciences, under Contract No. DE-AC02-98CH10886. The NIGMS East Coast Structural Biology Research Facility, the X6A beamline, is funded under contract #GM-0080.

## References

- Allaire, M., Aslantas, M., Berntson, A., Bermann, L., Cheung, S., Clay, B., Greene, R., Jakoncic, J., Johnson, E., Kao, C. C., Lenhard, A., Pjerov, S., Siddons, D. P., Stober, W., Venkatagiriappa, V., Yin, Z. & Stojanoff, V. (2003). *Synchrotron Radiat. News*, **16**, 20–25.
- Aslantas, M., Jakoncic, J., Honkimaki, V., Di Michiel, M., Zhong, Z., Siddons, D. P. & Stojanoff, V. (2007). In preparation.
- Arndt, U. W. (1984). *J. Appl. Cryst.* **17**, 118–119.
- Banumathi, S., Zwart, P., Ramagopal, U. A., Dauter, M. & Dauter, Z. (2004). *Acta Cryst.* **D60**, 1085–1093.
- Cassetta, A., Deacon, M. A., Ealick, S. E., Helliwell, J. R. & Thompson, A. W. (1999). *J. Synchrotron Rad.* **6**, 822–833.
- Chayen, N. E. (1998). *Acta Cryst.* **D54**, 8–15.
- Cianci, M., Helliwell, J. R., Helliwell, M., Kaucic, V., Logar, N. Z., Mali, G. & Tusar, N. N. (2005). *Crystallogr. Rev.* **11**, 245–335.
- Collaborative Computational Project, Number 4 (1994). *Acta Cryst.* **D50**, 760–763.
- Cowtan, K. (1994). *Int. CCP4/ESF-EAMCB Newsl. Protein Crystallogr.* **31**, 34–38.
- Dauter, Z. (2002). *Curr. Opin. Struct. Biol.* **12**, 674–678.
- Dauter, Z. & Adams, D. A. (2001). *Acta Cryst.* **D57**, 990–995.
- Dauter, Z. & Dauter, M. (1999). *J. Mol. Biol.* **289**, 93–101.
- Dauter, Z., Dauter, M., de la Fortelle, E., Bricogne, G. & Sheldrick, G. M. (1999). *J. Mol. Biol.* **289**, 83–92.
- Diederichs, K. (2006). *Acta Cryst.* **D62**, 96–101.
- Emsley, P. & Cowtan, K. (2004). *Acta Cryst.* **D60**, 2126–2132.
- Esnouf, R. M. (1997). *J. Mol. Graph.* **15**, 132–134.
- Evans, G. & Pettifer, R. F. (2001). *J. Appl. Cryst.* **34**, 82–86.
- Fourme, R., Girard, E., Kahn, R., Ascone, I., Mezouar, M., Dhaussy, A. C., Lin, T. & Johnson, J. E. (2003). *Acta Cryst.* **D59**, 1767–1772.
- Fourme, R. & Hendrickson, W. A. (1990). *Synchrotron Radiation and Biophysics*, edited by S. S. Hasnain, pp. 156–175. Chichester: Ellis Horwood.
- Fourme, R., Kahn, R., Mezouar, M., Girard, E., Hoerentrup, C., Prange, T. & Ascone, I. (2001). *J. Synchrotron Rad.* **8**, 1149–1156.
- Fourme, R., Shepard, W., Schiltz, M., Prangé, T., Ramin, M., Kahn, R., de la Fortelle, E. & Bricogne, G. (1999). *J. Synchrotron Rad.* **6**, 834–844.
- French, G. S. & Wilson, K. S. (1978). *Acta Cryst.* **A34**, 517–525.
- Girard, E., Kahn, R., Ascone, I., Mezouar, M., Dhaussy, A. C., Lin, T., Johnson, J. E. & Fourme, R. (2004). *High Pressure Res.* **24**, 173–182.
- González, A. (2003). *Acta Cryst.* **D59**, 315–322.
- Gonzalez, A., Denny, R. & Nave, C. (1994). *Acta Cryst.* **D50**, 276–282.
- Grosse-Kunstleve, R. W. & Adams, P. D. (2003). *Acta Cryst.* **D59**, 1966–1973.
- Helliwell, J. R. (1992). *Macromolecular Crystallography with Synchrotron Radiation*. Cambridge University Press.
- Helliwell, J. R., Ealick, S., Doing, P., Irving, T. & Szebenyi, M. (1993). *Acta Cryst.* **D49**, 120–129.
- Helliwell, J. R. & Fourme, R. (1983). ESRP Report IRI-4/83, 1–36. CERN, Geneva.
- Hendrickson, W. A. (1991). *Science*, **254**, 51–58.
- Hendrickson, W. A. (1999). *J. Synchrotron Rad.* **6**, 845–851.
- Hendrickson, W. A. & Teeter, M. M. (1981). *Nature (London)*, **290**, 107–113.
- Kraulis, P. J. (1991). *J. Appl. Cryst.* **24**, 946–950.
- Matthews, B. W. (1968). *J. Mol. Biol.* **33**, 491–497.
- Merritt, E. A. & Murphy, M. E. (1994). *Acta Cryst.* **D50**, 869–873.
- Murray, J. W. & Garman, E. F. (2002). *J. Synchrotron Rad.* **9**, 347–354.
- Murshudov, G. N., Vagin, A. A. & Dodson, E. J. (1997). *Acta Cryst.* **D53**, 240–255.
- Nanao, M. H., Sheldrick, G. M. & Ravelli, R. B. G. (2005). *Acta Cryst.* **D61**, 1227–1237.
- Ness, S. R., de Graaff, R. A. G., Abrahams, J. P. & Pannu, N. S. (2004). *Structure*, **12**, 1753–1761.
- O'Neill, P., Stevens, D. L. & Garman, F. (2002). *J. Synchrotron Rad.* **9**, 329–332.
- Otwinowski, Z. & Minor, W. (1997). *Methods Enzymol.* **276**, 307–326.
- Perrakis, A., Morris, R. & Lamzin, V. S. (1999). *Nature Struct. Biol.* **6**, 458–463.
- Peterson, M. R., Harrop, S. J., McSweeney, S. M., Leonard, G. A., Thompson, A. W., Hunter, W. N. & Helliwell, J. R. (1996). *J. Synchrotron Rad.* **3**, 24–34.
- Ramagopal, U. A., Dauter, M. & Dauter, Z. (2003). *Acta Cryst.* **D59**, 1020–1027.
- Ramagopal, U. A., Dauter, Z., Thirumuruhan, R., Fedorov, E. & Almo, S. C. (2005). *Acta Cryst.* **D61**, 1289–1298.
- Ravelli, R. B. G., Schröder-Leiros, H. K., Pan, B., Caffrey, M. & McSweeney, S. (2003). *Structure*, **11**, 217–224.
- Schiltz, M., Dumas, P., Ennifar, E., Flensburg, C., Paciorek, W., Vornrhein, C. & Bricogne, G. (2004). *Acta Cryst.* **D60**, 1024–1031.
- Schiltz, M., Kvick, A., Svensson, O. S., Shepard, W., de La Fortelle, E., Prange, T., Kahn, R., Bricogne, G. & Fourme, R. (1997). *J. Synchrotron Rad.* **4**, 287–297.
- Sheldrick, G. & Gould, R. O. (1995). *Acta Cryst.* **B51**, 423–431.
- Takeda, K., Miyatake, H., Park, S.-Y., Kawamoto, M., Kamiya, N. & Miki, K. (2004). *J. Appl. Cryst.* **37**, 925–933.
- Wang, B.-C. (1985). *Methods Enzymol.* **115**, 90–112.
- Zhong, Z., Kao, C. C., Siddons, D. P. & Hastings, J. B. (2001). *J. Appl. Cryst.* **34**, 504–509.
- Zwart, P. H., Banumathi, S., Dauter, M. & Dauter, Z. (2004). *Acta Cryst.* **D60**, 1958–1963.